Spin-orbit scattering in quantum diffusion of massive Dirac fermions

Wen-Yu Shan, Hai-Zhou Lu,* and Shun-Qing Shen
Department of Physics and Centre of Theoretical and Computational Physics, The University of Hong Kong, Pokfulam Road, Hong Kong, China

(Received 25 March 2012; revised manuscript received 31 July 2012; published 4 September 2012)

We theoretically study the effects of spin-orbit scattering on weak (anti)localization in two-dimensional massive Dirac systems. We clarify that weak antilocalization and localization of a single massive Dirac cone come from the diffusion of a singlet Cooperon in the massless limit and one of triplet Cooperons in the large-mass limit, respectively. Spin-orbit scattering behaves like random magnetic scattering to the triplet Cooperon, and suppresses the weak localization in the large-mass regime, different from in conventional systems where spin-orbit scattering leads to a crossover from weak localization to antilocalization. This behavior suggests an experiment to detect the weak localization of bulk subbands in topological insulator thin films, in which an enhancement of "weak antilocalization" is expected after doping heavy-element impurities. Finally, we compare the conventional electron and Dirac fermion systems in the quantum diffusion transport under ordinary, spin-orbit, and magnetic scattering.

DOI: 10.1103/PhysRevB.86.125303 PACS number(s): 73.25.+i, 03.65.Vf, 73.20.−r, 85.75.−d

I. INTRODUCTION

A key feature in magnetoresistance measurements of topological insulators (TIs)[1–3] is the weak antilocalization, which exhibits as a negative magnetoconductance in a small magnetic field.[4–14] The prevailing understanding to it is based on the π Berry phase of the massless surface states.[15,16] The π Berry phase gives a destructive quantum interference correction to backscattering, leading to a conductivity enhancement, that is, the weak antilocalization (WAL). WAL is not a stranger to conventional electrons. It also occurs in a number of metal and semiconductor systems with strong spin-orbit scattering,[17–20] where WAL is formulated by backscattering correlation functions, known as Cooperons[21] (examples of their Feynman diagrams are shown at the bottom of Fig. 1). Cooperons are functions of the summations of quantum numbers on their incoming and outgoing sides, thus they contribute sensitively to backscattering (momenta $\mathbf{k}_{\rm in}+\mathbf{k}_{\rm out}\sim 0$) and magnetoconductivity (effect of the magnetic vector potential $\mathbf{A}$ on canonical momentum $\mathbf{k}\to\mathbf{k}+e\mathbf{A}/\hbar$ is doubled $\to \mathbf{k}_{\rm in}+\mathbf{k}_{\rm out}+2e\mathbf{A}/\hbar$). Because of the double degeneracy, spin of a conventional two-dimensional electron can be either flipped or conserved after backscattering. The summation j of the spins before and after backscattering can be used as an index to characterize three spin-triplet ($j=1$) and one spin-singlet ($j=0$) Cooperons.[22,23] Diffusion of the singlet Cooperon leads to WAL, while the triplet Cooperons give weak localization (WL). Usually the triplet Cooperons outnumber the singlet Cooperon in conventional systems, and consequently the total effect exhibits WL. However, the triplets can be suppressed by strong spin-orbit scattering due to their nonzero spin, leaving only the singlet and accompanied WAL.[20,22–24]

In this work we study the effects of spin-orbit scattering on WAL and WL of massive Dirac fermions. Both the surface and bulk states in a topological thin film can be described by a two-dimensional Dirac model in the massless and large-mass limits, respectively. Their WAL and WL come from the "singlet Cooperon" in the massless limit and one of "triplet Cooperons" in the large-mass limit, respectively (see Fig. 1). Spin-orbit scattering behaves like random magnetic scattering, only to the triplet, and drastically suppresses WL of the bulk states in the large-mass regime. In contrast, it leaves WAL of the surface states almost unaffected. Different from conventional electrons, strong spin-orbit scattering cannot turn WL of Dirac fermion in the large-mass case into WAL. The picture is thereby unified in the language of Cooperon for conventional and massive Dirac fermions. We expect the suppression of WL to be observed by doping impurities of heavy nonmagnetic elements (e.g., Au) onto thin films of topological insulators.

The paper is organized as follows. In Sec. II we describe the massive Dirac model and the parameters to characterize spin-orbit scattering. In Sec. III we present the results directly. All the details of the calculations of the quantum interference (weak localization) correction to conductivity are presented in Sec. IV, where elastic, magnetic, and spin-orbit scattering are considered on the same footing. In Secs. III A and III B we compare the results of weak (anti)localization for the massive Dirac model, in the presence of weak and strong spin-orbit scattering. In Sec. III C we illustrate the physical picture in the language of Cooperons. In Sec. III D we propose an experiment to detect the weak localization from the bulk states of a topological insulator thin film, using the suppression of the weak localization from the triplet Cooperon by the spin-orbit scattering. Finally, a conclusion is given in Sec. V by comparing the conventional electron and Dirac fermion systems in the quantum diffusion transport under different scattering mechanisms.

II. MODEL

The massive Dirac model reads

$$H=\hbar v(\sigma_x k_y-\sigma_y k_x)+m\sigma_z, \tag{1}$$

where (k_x,k_y) is the wave vector, $(\sigma_x,\sigma_y,\sigma_z)$ are Pauli matrices, $\hbar$ is Planck's constant over 2π, v is the effective velocity, and m is the mass or energy gap. The equation can be used to describe the two-dimensional bulk[25] and surface bands[26–28] in the thin-film limit by introducing different model parameters. The simplified description for the bulk states is supported by a recent work that describes the bulk states with the three-dimensional Dirac model, where the weak localization of the bulk states was also found,[29] qualitatively consistent with our

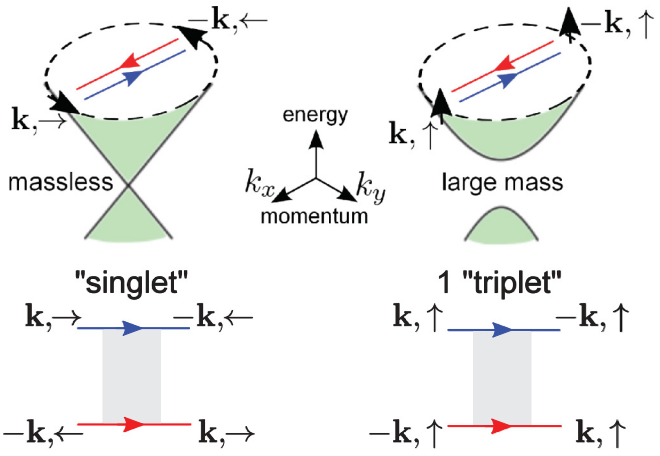

FIG. 1. (Color online) "Cooperons" for Dirac fermion. Top: Dirac cone and spin polarization (short arrows on dashed loops) on the Fermi surface, in the massless and large-mass limits, respectively. Bottom: Corresponding "Cooperon" Feynman diagrams for weak (anti)localization. They depict the correlation of backscattering events (i.e., momentum $\mathbf{k}$ becomes $-\mathbf{k}$, long arrowed lines). At the four corners, $\pm\mathbf{k},\rightleftarrows/\uparrow$ represent the states of scattered electrons. The mass of Dirac cone determines the spin polarization on the Fermi surface. In the massless limit, spin is in-plane and locked to momentum. Spin must be flipped after backscattering, so the summation of the incoming spin and outgoing spin is 0 ("singlet Cooperon"). In the large-mass limit, spin is out of plane and independent on momentum. Spin remains unchanged after backscattering, so the total spin is 1 ("triplet Cooperon").

previous conclusion.[25] Spin-orbit scattering is characterized by a length $\ell_{\rm so}$. Shorter $\ell_{\rm so}$ means stronger spin-orbit scattering. $\ell_{\rm so}$ is related to the spin-orbit scattering time $\tau_{\rm so}$ by $\ell_{\rm so} = \sqrt{D\tau_{\rm so}}$, where D is the diffusion constant. The total scattering time $\tau_{\rm so}$ is given by $1/\tau_{\rm so} = 2/\tau_{{\rm so},x} + 1/\tau_{{\rm so},z}$, where $\tau_{{\rm so},x}$ and $\tau_{{\rm so},z}$ are its in-plane and out-of-plane components, respectively. The Dirac model and spin-orbit scattering are intrinsic and extrinsic consequences of spin-orbit interaction,[30] respectively (see Table I).

III. RESULTS

Weak (anti)localization exhibits as: (i) a positive (negative) logarithmic magnetoconductivity or (ii) a suppressed (enhanced) quantum conductivity at low temperatures in the metallic regime. They originate from the quantum interference correction to conductivity, and can be calculated by the diagrammatic techniques.[17,20,31–35] We obtain the quantum conductivity and magnetoconductivity in the presence of spin-orbit scattering (see Sec. IV). Their formulas (in Secs. IV G and IV H) are of the same structures as those with only elastic and magnetic scatterings,[36] but the crucial difference is that all the relaxation times from the spin-orbit scattering have the opposite signs with respect to those from the magnetic scattering: $1/\tau_x \to 1/\tau_x - 1/\tau_{{\rm so},x}$ and $1/\tau_z \to 1/\tau_z - 1/\tau_{{\rm so},z}$, where $\tau_{x/z}$ are magnetic scattering times. This sign change reflects the difference between the unitary symmetry of the magnetic scattering and the symplectic symmetry of the spin-orbit scattering. The total scattering time τ now is given by $1/\tau = 1/\tau_e + 1/\tau_m + 1/\tau_{\rm so}$, τ_e is the elastic scattering time.

TABLE I. Consequences of spin-orbit interaction. v and m are the velocity and mass, respectively, in the Dirac model. $\ell_{\rm so}$ and $\tau_{\rm so}$ are the spin-orbit scattering length and time, respectively. Shorter $\ell_{\rm so}$ means stronger spin-orbit scattering.

	Intrinsic (uniform)	Extrinsic (random)
Hamiltonian	Dirac model	Spin-orbit scattering
Parameter	v and m	$\ell_{\rm so}$, $\tau_{\rm so}$

A. Weak spin-orbit scattering

We first review the results in the absence of spin-orbit scattering ($\ell_{\rm so} \to \infty$). The massive Dirac model in Eq. (1) carries a Berry phase

$$\gamma = \pi\left(1 - \frac{m}{\sqrt{m^2 + (v\hbar k_F)^2}}\right),$$

where k_F is the Fermi wave vector. The Berry phase γ can be tuned from π to 0 as m varies from 0 to $\gg \hbar v k_F$, corresponding to the massless and large-mass limits, respectively. In the massless limit, the destructive interference due to the π Berry phase leads to WAL.[33] In the large-mass limit ($\gamma \to 0$), the quantum interference is reversed, giving rise to WL.[11,36,37]

B. Strong spin-orbit scattering

Inclusion of spin-orbit scattering will suppress WL in the large-mass regime. Figures 2(a) and 2(b) show the magnetoconductivity with weak ($\ell_{\rm so} = 10\,000$ nm) and strong ($\ell_{\rm so} = 300$ nm) spin-orbit scattering, respectively. WAL can be recognized as negative curves, while WL as positive curves. Comparing Figs. 2(a) and 2(b), the WAL curves in small-mass regime ($\gamma/\pi = 1, 0.9, 0.75$) are almost unaffected, while the WL curves in the large-mass regime ($\gamma/\pi = 0.5, 0.1, 0.001$) are suppressed. Especially, WL totally vanishes in the limit $\gamma \to 0$. Figure 2(c) shows the quantum conductivity $\sigma^F(0)$ as a function of γ and $\ell_{\rm so}$. Positive $\sigma^F(0)$ means WAL and negative $\sigma^F(0)$ means WL. The dashed curve separates the WAL and WL regimes. Without spin-orbit scattering ($\ell_{\rm so} \to \infty$), both WAL and WL regimes exist. Increasing spin-orbit scattering (decreasing $\ell_{\rm so}$) shrinks the WL regime. In the limit of strong spin-orbit scattering ($\ell_{\rm so} \to 0$), the WL regime vanishes totally.

The suppression of WL by spin-orbit scattering can be further examined from the effective phase coherence lengths. WL or WAL happens because an electron can be scattered by static centers many times but still maintains its phase. The phase is protected by long phase coherence length. In our calculation, the WL-WAL crossover can always be described by two competing terms, one for WL and the other for WAL. Each term is characterized by an effective phase coherence length, denoted as $\ell_{\rm L}$ and $\ell_{\rm AL}$, respectively. For weak spin-orbit scattering ($\ell_{\rm so} \to \infty$), the WL phase coherence length $\ell_{\rm L}$ diverges as $\gamma \to 0$ [see dashed curves in Fig. 3(a)]. The divergence of $\ell_{\rm L}$ protects WL in the large-mass limit ($\gamma \to 0$). For strong spin-orbit scattering ($\ell_{\rm so} \to 0$), $\ell_{\rm L}$ in the large-mass regime is shortened [the solid curve in Fig. 3(a)]. Figure 3(b) shows $\ell_{\rm L}$ as a function of $\ell_{\rm so}$ in the large-mass limit. The

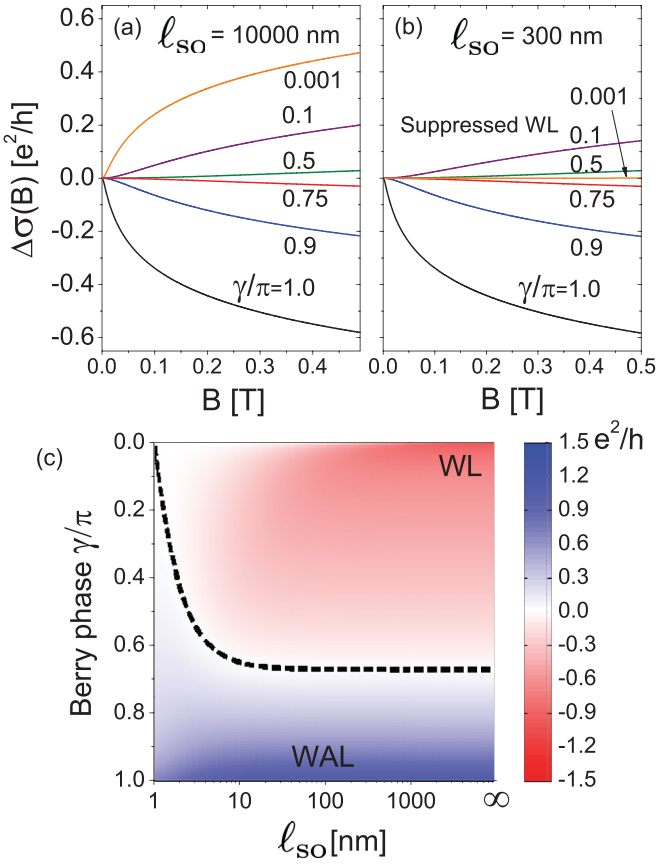

FIG. 2. (Color online) (a) and (b) Magnetoconductivity $\Delta\sigma(B)$ for different Berry phase γ and with: (a) weak spin-orbit scattering (spin-orbit scattering length $\ell_{so} = 10\,000$ nm) and (b) strong spin-orbit scattering ($\ell_{so} = 300$ nm). $\gamma/\pi = 1$ in the massless limit and 0 in the large-mass limit. (c) Zero-field quantum conductivity $\sigma^F(0)$ (in units of e^2/h, color bar on the right). The dashed curve separates the positive WAL and negative WL regimes. Other parameters: elastic scattering length $\ell_e = 10$ nm and phase coherence length $\ell_\phi = 300$ nm.

slope of the curves becomes steeper as the mass increases (i.e., γ decreases), showing that spin-orbit scattering has stronger influence on larger mass cases. In the $\gamma \to 0$ limit, $\ell_L \to 0$ as $\ell_{so} \to 0$, leading to the vanishing magnetoconductivity in Fig. 2(b).

C. Physical picture in the language of Cooperons

The suppression of WL can be interpreted in the language of Cooperon. The quantum conductivity is proportional to

$$\sigma^F \sim \sum_{\mathbf{q}} \Gamma(\mathbf{q}),$$

where the Cooperon vertex function Γ is a function of $\mathbf{q}$, the summation of incoming and outgoing momenta, and can be found by the diagrammatic calculation as [Eq. (37)]

$$\Gamma(\mathbf{q}) \approx \Gamma^{(0)} + \Gamma^{(1)} e^{i(\varphi_{\mathbf{k}} - \varphi_{\mathbf{q}-\mathbf{k}})}, \tag{2}$$

where $\varphi_{\mathbf{k}}$ and $\varphi_{\mathbf{q}-\mathbf{k}}$ are momentum angles for incoming and outgoing states. $\Gamma^{(0)}$ gives WL. For backscattering $\mathbf{q} \to 0$, then $e^{i(\varphi_{\mathbf{k}} - \varphi_{\mathbf{q}-\mathbf{k}})} \approx e^{i\pi} = -1$, thus $\Gamma^{(1)}$ term is related to the π Berry phase and gives an opposite contribution to $\Gamma^{(0)}$ (i.e.,

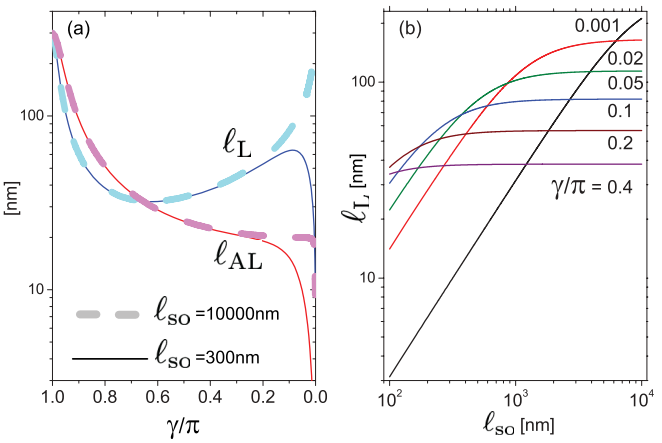

FIG. 3. (Color online) (a) The weak antilocalization phase coherence length (ℓ_{AL}, red and magenta) and the weak localization phase coherence length (ℓ_L, blue and cyan) as a function of Berry phase γ for weak ($\ell_{so} = 10\,000$ nm) and strong ($\ell_{so} = 300$ nm) spin-orbit scattering. $\gamma/\pi = 1$ in the massless limit and 0 in the large-mass limit. (b) The weak localization phase coherence length ℓ_L as a function of the spin-orbit scattering length ℓ_{so} in the large-mass regime ($\gamma/\pi \leqslant 0.4$).

WAL).[33,38] On the other side, if we regard the Cooperon vertex function as an operator $\hat{\Gamma}$ acting on the states at its four corners (see Fig. 1), $\Gamma^{(0)}$ and $\Gamma^{(1)}$ in Eq. (2) are found as (see Sec. IV I)

$$\Gamma^{(0)} = \cos^4\frac{\theta}{2}\langle 1,1|\hat{\Gamma}|1,1\rangle, \quad \Gamma^{(1)} = \frac{1}{2}\sin^2\theta\langle 0,0|\hat{\Gamma}|0,0\rangle,$$

where $|j,m\rangle$ labels the total spin of incoming and outgoing states and its z component,[24,39] respectively. $\cos\theta \equiv m/\sqrt{m^2 + (\hbar v k_F)^2}$. Therefore, $\Gamma^{(0)}$ is from one of the triplets, while $\Gamma^{(1)}$ is from the singlet. These two limits (massless and large mass) are shown in Fig. 1. These mass-dependent Cooperons are similar to the "soft" Cooperon modes of the bulk states in a recent work.[29]

In the absence of spin-orbit scattering, $\Gamma^{(0)}$ and $\Gamma^{(1)}$ diverge as $1/q^2$, respectively, in the large-mass and massless limits, leading to the WL and WAL in Fig. 2. By adding spin-orbit scattering, $\Gamma^{(0)}$ becomes suppressed since it is not invariant under SU(2) rotation in the total spin space.[23] In other words, spin-orbit scattering behaves like random magnetic scattering only to the triplet Cooperon, giving rise to the suppression of WL.

D. Experiment to detect the localization from the bulk states

The suppression of WL by spin-orbit scattering suggests an experiment to detect WL of bulk states in topological insulator thin films. It is known that both the bulk and surface states contribute to the transport in as-grown topological insulators.[40,41] In a thin film of a topological insulator, the three-dimensional bulk states split into a series of two-dimensional subbands. If the film is thin enough, only the lowest bulk subbands cross the Fermi energy. This case is shown in Fig. 4(b). Both the surface states and bulk states in a topological insulator thin film can be described by the same massive Dirac model, with the surface states in the massless limit and the bulk states in the large-mass regime. Therefore, unlike in other

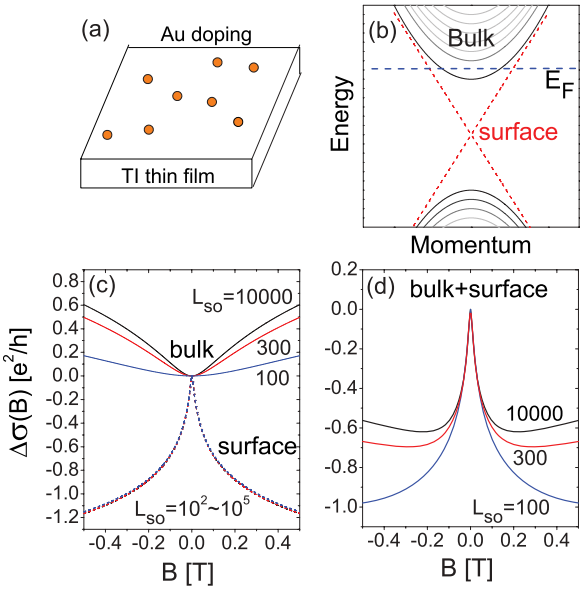

FIG. 4. (Color online) (a) A topological insulator thin film doped with impurities that bring strong spin-orbit scattering (e.g., Au). (b) Schematic description of the band structure of a thin film of a topological insulator. Solid and dashed lines depict the bulk subbands and surface states, respectively. E_F is the Fermi energy. Each solid line represents a pair of bulk subbands. (c) Surface and bulk contributions to the magnetoconductivity before ($\ell_{so} = 10\,000$ nm) and after ($\ell_{so} = 300, 100$ nm) Au impurities are doped. In the simulation, one surface band (with $\gamma = \pi$) and two bulk subbands (with $\gamma = 0.15\pi$) are assumed. (d) The total magnetoconductivity from the surface states and bulk subbands before and after Au impurities are doped. The spin-orbit scattering length is in units of nanometers.

systems with strong spin-orbit coupling, the bulk states in the topological insulator could give WL that neutralizes WAL from the surface states [Fig. 4(c)]. The observed WAL-like negative magnetoconductivity actually comes from the summation of the stronger WAL from the surface states and WL from the bulk states. Introducing impurities that can bring spin-orbit scattering will suppress WL from the large-mass bulk states, but not affect WAL from the massless surface states. Overall speaking, one will expect an enhancement of WAL as shown in Fig. 4(d). The recent experiment on the five quintuple-layer Bi_2Te_3 thin film with Au impurities may have already implied the effect.[8]

IV. DIAGRAMMATIC TECHNIQUES

In this section we present the calculation of the quantum interference (weak localization) correction to conductivity with the help of the diagrammatic techniques. Although this work focuses on the spin-orbit scattering, the magnetic scattering is also included in the calculation.

A. Eigenstates

The two-dimensional massive Dirac Hamiltonian in Eq. (1) describes a conduction band and a valence band. We suppose that the Fermi level E_F intersects with only the conduction band, and in the limit of weak scattering $E_F \gg \hbar/\tau$, the valence band becomes irrelevant for transport, where τ is the total scattering time. The dispersion of the conduction band is

$$\epsilon_{\mathbf{k}} = \sqrt{m^2 + \hbar^2 v^2 k^2} \tag{3}$$

and its wave function is given by

$$\langle \mathbf{r}|\mathbf{k}\rangle = \psi_{c,\mathbf{k}}(\mathbf{r}) = \frac{1}{\sqrt{S}} \begin{pmatrix} a \\ -ibe^{i\varphi_{\mathbf{k}}} \end{pmatrix} e^{i\mathbf{k}\cdot\mathbf{r}}, \tag{4}$$

where S is the area, $\tan\varphi_{\mathbf{k}} \equiv k_y/k_x$, $a = \cos\frac{\theta}{2}$, $b = \sin\frac{\theta}{2}$, and $\cos\theta = m/E_F$. The Fermi energy E_F is measured from the Dirac point.

B. Impurity potentials

The impurity potentials are given by

$$U(\mathbf{r}) = U_0(\mathbf{r}) + U_m(\mathbf{r}) + U_{so}(\mathbf{r}), \tag{5}$$

where $U_0(\mathbf{r})$ is for the elastic scattering, $U_m(\mathbf{r})$ is for the magnetic scattering, $U_{so}(\mathbf{r})$ is for the spin-orbit scattering, and

$$\begin{aligned} U_0(\mathbf{r}) &= \sum_i u_0^i \delta(\mathbf{r} - \mathbf{R}_i), \\ U_m(\mathbf{r}) &= \sum_i \sum_{\alpha=x,y,z} u_\alpha^i \sigma_\alpha \delta(\mathbf{r} - \mathbf{R}_i), \\ U_{so}(\mathbf{r}) &= \sum_i \frac{\hbar}{4m^2c^2} \vec{\sigma} \cdot \nabla u(\mathbf{r} - \mathbf{R}_i) \times \mathbf{p}, \end{aligned} \tag{6}$$

where $u(\mathbf{r} - \mathbf{R}_i)$ represents the random potential by an impurity located at $\mathbf{R}_i$. $\vec{\sigma} = (\sigma_x, \sigma_y, \sigma_z)$ is the vector of Pauli matrices.

The scattering (Born) amplitude $U_{\mathbf{k},\mathbf{k}'}$ can be found as

$$\begin{aligned} U_{\mathbf{k},\mathbf{k}'} &\equiv \langle \mathbf{k}|U(\mathbf{r})|\mathbf{k}'\rangle \\ &= \langle \mathbf{k}|U_0(\mathbf{r})|\mathbf{k}'\rangle + \langle \mathbf{k}|U_m(\mathbf{r})|\mathbf{k}'\rangle + \langle \mathbf{k}|U_{so}(\mathbf{r})|\mathbf{k}'\rangle, \end{aligned} \tag{7}$$

where for the elastic scattering

$$\langle \mathbf{k}|U_0(\mathbf{r})|\mathbf{k}'\rangle = \frac{1}{S} \sum_i u_0^i e^{i(\mathbf{k}'-\mathbf{k})\cdot\mathbf{R}_i} (a^2 + b^2 e^{i(\varphi_{\mathbf{k}'} - \varphi_{\mathbf{k}})}), \tag{8}$$

for the magnetic scattering

$$\begin{aligned} &\langle \mathbf{k}|U_m(\mathbf{r})|\mathbf{k}'\rangle \\ &= \sum_i \frac{1}{S} e^{i(\mathbf{k}'-\mathbf{k})\cdot\mathbf{R}_i} \big[i u_x^i ab(e^{-i\varphi_{\mathbf{k}}} - e^{i\varphi_{\mathbf{k}'}}) \\ &\quad - u_y^i ab(e^{i\varphi_{\mathbf{k}'}} + e^{-i\varphi_{\mathbf{k}}}) + u_z^i (a^2 - b^2 e^{i(\varphi_{\mathbf{k}'} - \varphi_{\mathbf{k}})}) \big], \end{aligned} \tag{9}$$

and for the spin-orbit scattering

$$\begin{aligned} \langle \mathbf{k}|U_{so}(\mathbf{r})|\mathbf{k}'\rangle &= \frac{1}{S} \int d\mathbf{r} (a, ibe^{-i\varphi_{\mathbf{k}}}) e^{i(\mathbf{k}'-\mathbf{k})\cdot\mathbf{r}} \sum_i \frac{\hbar^2}{4m^2c^2} \\ &\quad \times \boldsymbol{\sigma} \cdot [\nabla u(\mathbf{r} - \mathbf{R}_i) \times \mathbf{k}'] \begin{pmatrix} a \\ -ibe^{i\varphi_{\mathbf{k}'}} \end{pmatrix} \\ &\equiv \frac{1}{S} \sum_i i u_{so}^i e^{i(\mathbf{k}'-\mathbf{k})\cdot\mathbf{R}_i} (a, ibe^{-i\varphi_{\mathbf{k}}}) \\ &\quad \times \boldsymbol{\sigma} \cdot (\mathbf{k} \times \mathbf{k}') \begin{pmatrix} a \\ -ibe^{i\varphi_{\mathbf{k}'}} \end{pmatrix} \\ &= \sum_i \frac{i u_{so}^i}{S} e^{i(\mathbf{k}'-\mathbf{k})\cdot\mathbf{R}_i} [iab(e^{-i\varphi_{\mathbf{k}}} - e^{i\varphi_{\mathbf{k}'}})(\mathbf{k} \times \mathbf{k}')_x \end{aligned}$$

$$- ab(e^{-i\varphi_{\mathbf{k}}} + e^{i\varphi_{\mathbf{k}'}})(\mathbf{k}\times\mathbf{k}')_y$$
$$+ (a^2 - b^2 e^{i(\varphi_{\mathbf{k}'}-\varphi_{\mathbf{k}})})(\mathbf{k}\times\mathbf{k}')_z], \quad (10)$$

where we have assumed the δ potential $\frac{\hbar^2}{4m^2c^2}u(\mathbf{r}-\mathbf{R}_i) = u_{\rm so}^i\delta(\mathbf{r}-\mathbf{R}_i)$.

C. Green's functions and relaxation times

The retarded (R) and advanced (A) Green's functions have the form

$$G_{\mathbf{k}}^{R/A}(\omega) = \frac{1}{\omega - \epsilon_{\mathbf{k}} \pm i\frac{\hbar}{2\tau}}, \quad (11)$$

where the disorder-induced self-energy is described by the relaxation time τ, which has the form

$$\frac{1}{\tau} = \frac{2\pi}{\hbar}\sum_{\mathbf{k}'}\langle U_{\mathbf{k}\mathbf{k}'}U_{\mathbf{k}'\mathbf{k}}\rangle_{\rm imp}\delta(E_F - \epsilon_{\mathbf{k}'}) \quad (12)$$

under the first-order Born approximation (see Fig. 5).

The correlation function in Eq. (12) is evaluated as

$$\langle U_{\mathbf{k}\mathbf{k}'}U_{\mathbf{k}'\mathbf{k}}\rangle_{\rm imp} = \frac{n_0u_0^2}{S}[a^4+b^4+2a^2b^2\cos(\varphi_{\mathbf{k}}-\varphi_{\mathbf{k}'})]$$
$$+\frac{t_x}{S}(2a^2b^2)[1-\cos(\varphi_{\mathbf{k}}+\varphi_{\mathbf{k}'})]$$
$$+\frac{t_y}{S}(2a^2b^2)[1+\cos(\varphi_{\mathbf{k}}+\varphi_{\mathbf{k}'})]$$
$$+\frac{t_z}{S}[a^4+b^4-2a^2b^2\cos(\varphi_{\mathbf{k}}-\varphi_{\mathbf{k}'})], \quad (13)$$

with

$$t_i = n_m u_i^2 + n_{\rm so}u_{\rm so}^2(\mathbf{k}\times\mathbf{k}')_i^2, \quad i = x,y,z, \quad (14)$$

where n_0, n_m, and $n_{\rm so}$ represent concentrations of nonmagnetic, magnetic, and spin-orbit impurities, respectively. u_0, $u_{x,y,z}$, $u_{\rm so}$ are their spatially averaged strengthes. The correlation between different types of scattering or different components of the same type is neglected. Therefore the relaxation time can be given according to different scattering mechanisms

$$\frac{1}{\tau_e} = \frac{2\pi N_F}{\hbar}n_0u_0^2(a^4+b^4),$$
$$\frac{1}{\tau_z} = \frac{2\pi N_F}{\hbar}n_mu_z^2(a^4+b^4),$$
$$\frac{1}{\tau_x} = \frac{1}{\tau_y} = \frac{2\pi N_F}{\hbar}n_mu_x^2(2a^2b^2), \quad (15)$$
$$\frac{1}{\tau_{{\rm so},z}} = \frac{2\pi N_F}{\hbar}(a^4+b^4)n_{\rm so}u_{{\rm so},z}^2\overline{(\mathbf{k}\times\mathbf{k}')_z^2},$$
$$\frac{1}{\tau_{{\rm so},x}} = \frac{1}{\tau_{{\rm so},y}} = \frac{2\pi N_F}{\hbar}(2a^2b^2)n_{\rm so}u_{{\rm so},x}^2\overline{(\mathbf{k}\times\mathbf{k}')_x^2},$$

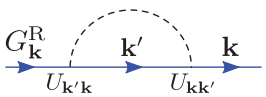

FIG. 5. (Color online) The retarded Green's function with its self-energy given by the first-order Born approximation. The solid and dash lines represent electron Green's function and impurity scattering, respectively.

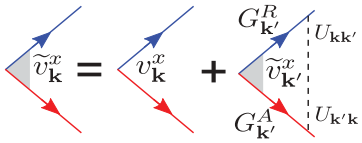

FIG. 6. (Color online) The ladder diagram correction to velocity. $v_{\mathbf{k}}^x$ and $\tilde{v}_{\mathbf{k}}^x$ label the bare and dressed velocities, respectively. The blue (red) line represents retarded (advanced) Green's function G^R (G^A).

where the in-plane isotropy has been assumed, and $(\mathbf{k}\times\mathbf{k}')_i^2$ are replaced by their average $\overline{(\mathbf{k}\times\mathbf{k}')_i^2}$.[17] In this way, τ in Eq. (11) is given by

$$\frac{1}{\tau} = \frac{1}{\tau_e} + \frac{1}{\tau_m} + \frac{1}{\tau_{\rm so}},$$
$$\frac{1}{\tau_m} = \frac{1}{\tau_{m,x}} + \frac{1}{\tau_{m,y}} + \frac{1}{\tau_{m,z}}, \quad (16)$$
$$\frac{1}{\tau_{\rm so}} = \frac{1}{\tau_{{\rm so},x}} + \frac{1}{\tau_{{\rm so},y}} + \frac{1}{\tau_{{\rm so},z}}.$$

D. Ladder diagram correction to velocity

For Dirac fermions, the ladder diagram correction to velocity (see Fig. 6) should be considered. The diagram describes the iterative equation for the corrected velocity $\tilde{v}_{\mathbf{k}}^x$,

$$\tilde{v}_{\mathbf{k}}^x = v_{\mathbf{k}}^x + \sum_{\mathbf{k}'}G_{\mathbf{k}'}^RG_{\mathbf{k}'}^A\langle U_{\mathbf{k}',\mathbf{k}}U_{\mathbf{k},\mathbf{k}'}\rangle_{\rm imp}\tilde{v}_{\mathbf{k}'}^x, \quad (17)$$

which leads to a correction η_v to the bare velocity $v_{\mathbf{k}}^x$,

$$\tilde{v}_{\mathbf{k}}^x = \eta_v v_{\mathbf{k}}^x, \quad (18)$$

where the bare velocity $v_{\mathbf{k}}^x = v\sin\theta\cos\varphi_{\mathbf{k}}$ and the correction factor

$$\eta_v = \frac{1}{1+\frac{a^2b^2}{a^4+b^4}(\tau/\tau_{{\rm so},z}+\tau/\tau_z-\tau/\tau_e)}. \quad (19)$$

E. Bare and dressed Hikami boxes

The quantum interference correction to conductivity involves the calculation of bare Hikami box in Fig. 7 and the dressed Hikami boxes in Fig. 8. At zero temperature, the bare Hikami box (Fig. 7) can be calculated as

$$\sigma_0^F = \frac{e^2\hbar}{2\pi S}\sum_{\mathbf{q}}\Gamma(\mathbf{q})\sum_{\mathbf{k}}\tilde{v}_{\mathbf{k}}^x\tilde{v}_{\mathbf{q}-\mathbf{k}}^xG_{\mathbf{k}}^RG_{\mathbf{k}}^AG_{\mathbf{q}-\mathbf{k}}^RG_{\mathbf{q}-\mathbf{k}}^A, \quad (20)$$

where the vertex function $\Gamma(\mathbf{q})$ depends only on the total incoming momentum $\mathbf{q}$, and the contribution from small $\mathbf{q}$

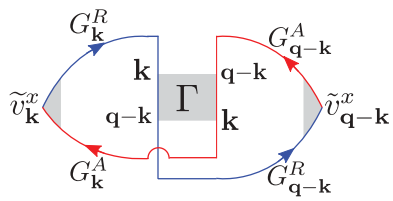

FIG. 7. (Color online) The bare Hikami box. The blue (red) line represents retarded (advanced) Green's function.

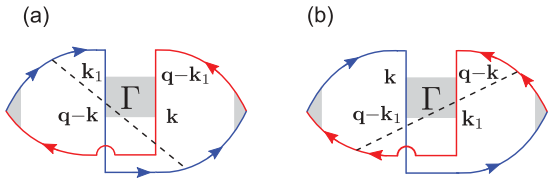

FIG. 8. (Color online) The retarded (a) and advanced (b) dressed Hikami boxes.

dominates the summation. Approximately, we can take $\mathbf{k}$ summation for $\mathbf{q}=0$ first and get

$$\sigma_0^F = -\frac{e^2v^2\eta_v^2 N_F\tau^3}{\hbar^2}\sin^2\theta\sum_{\mathbf{q}}\Gamma(\mathbf{q}). \tag{21}$$

For Dirac fermions, two dressed Hikami boxes (see Fig. 8) should also be considered. We denote them as σ_R^F and σ_A^F, and their diagrams can be calculated as

$$\begin{aligned}\sigma_R^F &= \frac{e^2\hbar}{2\pi S}\sum_{\mathbf{q}}\Gamma(\mathbf{q})\sum_{\mathbf{k}}\sum_{\mathbf{k_1}}\tilde{v}^x_{\mathbf{k}}\tilde{v}^x_{\mathbf{q-k_1}}G^R_{\mathbf{k}}G^R_{\mathbf{k_1}}G^R_{\mathbf{q-k}}\\ &\quad\times G^R_{\mathbf{q-k_1}}G^A_{\mathbf{k}}G^A_{\mathbf{q-k_1}}\langle U_{\mathbf{k_1},\mathbf{k}}U_{\mathbf{q-k_1},\mathbf{q-k}}\rangle_{\rm imp},\end{aligned} \tag{22}$$

$$\begin{aligned}\sigma_A^F &= \frac{e^2\hbar}{2\pi S}\sum_{\mathbf{q}}\Gamma(\mathbf{q})\sum_{\mathbf{k}}\sum_{\mathbf{k_1}}\tilde{v}^x_{\mathbf{k}}\tilde{v}^x_{\mathbf{q-k_1}}G^R_{\mathbf{k}}G^R_{\mathbf{q-k_1}}G^A_{\mathbf{k}}\\ &\quad\times G^A_{\mathbf{k_1}}G^A_{\mathbf{q-k}}G^A_{\mathbf{q-k_1}}\langle U_{\mathbf{k},\mathbf{k_1}}U_{\mathbf{q-k},\mathbf{q-k_1}}\rangle_{\rm imp},\end{aligned} \tag{23}$$

and we have

$$\sigma_R^F = \sigma_A^F = -\frac{e^2v^2\eta_v^2 N_F\tau^3}{\hbar^2}\eta_H\sin^2\theta\sum_{\mathbf{q}}\Gamma(\mathbf{q}), \tag{24}$$

with

$$\eta_H = -\frac{1}{2}\left[\frac{a^2b^2}{a^4+b^4}\left(\frac{\tau}{\tau_e}-\frac{\tau}{\tau_z}+\frac{\tau}{\tau_{{\rm so},z}}\right)-\frac{\tau}{\tau_x}+\frac{\tau}{\tau_{{\rm so},x}}\right]. \tag{25}$$

The total contribution is given by the summation of three diagrams in Figs. 7 and 8,

$$\begin{aligned}\sigma^F &= \sigma_0^F+\sigma_R^F+\sigma_A^F\\ &= -\frac{e^2v^2\eta_v^2N_F\tau^3}{\hbar^2}\sin^2\theta(1+2\eta_H)\sum_{\mathbf{q}}\Gamma(\mathbf{q}).\end{aligned} \tag{26}$$

F. Bethe-Salpeter equation

Now the main task is to derive the vertex function $\Gamma(\mathbf{q})$ for the maximally crossed diagrams. First we need to evaluate the bare vertex $\Gamma^0(\mathbf{q})$, which has the form

$$\begin{aligned}\Gamma^0_{\mathbf{k}_\alpha\mathbf{k}_\beta} &\equiv \langle U_{\mathbf{k}_\beta,\mathbf{k}_\alpha}U_{\mathbf{q-k}_\beta,\mathbf{q-k}_\alpha}\rangle_{\rm imp}\\ &\approx \frac{\hbar}{2\pi N_F\tau S}(A+Be^{i(\varphi_\alpha-\varphi_\beta)}+Ce^{2i(\varphi_\alpha-\varphi_\beta)}),\end{aligned} \tag{27}$$

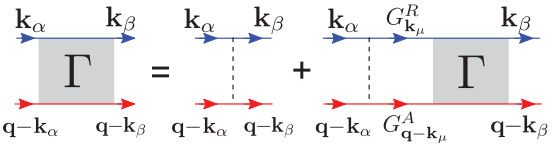

FIG. 9. (Color online) The Bethe-Salpeter equation for the vertex of maximally crossed diagrams.

in the limit $\mathbf{q}\to 0$, where

$$\begin{aligned}A &= \frac{a^4}{a^4+b^4}\left(\frac{\tau}{\tau_e}+\frac{\tau}{\tau_z}-\frac{\tau}{\tau_{{\rm so},z}}\right),\\ B &= \frac{2a^2b^2}{a^4+b^4}\left(\frac{\tau}{\tau_e}-\frac{\tau}{\tau_z}+\frac{\tau}{\tau_{{\rm so},z}}\right)-2\left(\frac{\tau}{\tau_x}-\frac{\tau}{\tau_{{\rm so},x}}\right),\\ C &= \frac{b^4}{a^4+b^4}\left(\frac{\tau}{\tau_e}+\frac{\tau}{\tau_z}-\frac{\tau}{\tau_{{\rm so},z}}\right).\end{aligned} \tag{28}$$

The full vertex function $\Gamma(\mathbf{q})$ is related to $\Gamma^0(\mathbf{q})$ by the Bethe-Salpeter equation (see Fig. 9),

$$\Gamma_{\mathbf{k}_\alpha\mathbf{k}_\beta} = \Gamma^0_{\mathbf{k}_\alpha\mathbf{k}_\beta}+\sum_{\mathbf{k}_\mu}\Gamma^0_{\mathbf{k}_\alpha\mathbf{k}_\mu}G^R_{\mathbf{k}_\mu}G^A_{\mathbf{q-k}_\mu}\Gamma_{\mathbf{k}_\mu\mathbf{k}_\beta}, \tag{29}$$

with $\mathbf{k}_{\alpha,\beta}$ labeling the independent incoming and outgoing momenta, respectively. This equation can be solved by expanding $\Gamma(\mathbf{q})$ and $\Gamma^0(\mathbf{q})$ into

$$\begin{aligned}\Gamma_{\mathbf{k}_\alpha\mathbf{k}_\beta} &= \frac{\hbar}{2\pi N_F\tau S}\sum_{n,m\in 0,1,2}Z_{nm}e^{i(n\varphi_\alpha-m\varphi_\beta)},\\ \Gamma^0_{\mathbf{k}_\alpha\mathbf{k}_\beta} &= \frac{\hbar}{2\pi N_F\tau S}\sum_{n,m\in 0,1,2}z_{nm}e^{i(n\varphi_\alpha-m\varphi_\beta)}.\end{aligned} \tag{30}$$

If we further define that

$$\Phi_{nm} = \frac{1}{2\pi}\int_0^{2\pi}d\varphi_\mu\frac{e^{i(m-n)\varphi_\mu}}{1+i\tau\mathbf{q}\cdot\mathbf{v}_\mu}, \quad n,m=0,1,2, \tag{31}$$

the expansion coefficients can be obtained in a matrix form

$$\mathbf{Z} = (\mathbf{I}-\mathbf{z}\mathbf{\Phi})^{-1}\mathbf{z}, \tag{32}$$

where

$$\mathbf{z} = \begin{pmatrix}A & 0 & 0\\ 0 & B & 0\\ 0 & 0 & C\end{pmatrix} \tag{33}$$

and up to q^2 terms in the small $\mathbf{q}$ limit

$$\mathbf{\Phi} \approx \begin{pmatrix}1-\frac{Q^2}{2} & -\frac{iQ_+}{2} & -\frac{Q_+^2}{4}\\ -\frac{iQ_-}{2} & 1-\frac{Q^2}{2} & -\frac{iQ_+}{2}\\ -\frac{Q_-^2}{4} & -\frac{iQ_-}{2} & 1-\frac{Q^2}{2}\end{pmatrix}, \tag{34}$$

with $Q^2=Q_x^2+Q_y^2$, $Q_\pm = Q_x\pm iQ_y$, and $\mathbf{Q}=v\tau\sin\theta\mathbf{q}$. Two diagonal terms of $\mathbf{Z}$ can be found as

$$\begin{aligned}Z_{00} &= \frac{2}{g_0+\left(1+\frac{1}{g_1}\right)Q^2},\\ Z_{11} &= \frac{2}{g_1+\left(1+\frac{1}{g_0}+\frac{1}{g_2}\right)Q^2},\end{aligned} \tag{35}$$

where the "Cooperon gaps" have been introduced

$$\begin{aligned} g_0 &= 2(1-A)/A, \\ g_1 &= 2(1-B)/B, \\ g_2 &= 2(1-C)/C, \end{aligned} \tag{36}$$

and Z_{22} has been omitted because it always has a nonvanishing Cooperon gap.

Put Eq. (35) into Eq. (30) and let $\mathbf{k}_\alpha = \mathbf{k}$ and $\mathbf{k}_\beta = \mathbf{q} - \mathbf{k}$, the vertex is found as

$$\Gamma_{\mathbf{k}_\alpha \mathbf{k}_\beta} \to \Gamma_{\mathbf{k}}(\mathbf{q}) \approx \Gamma^{(0)} + \Gamma^{(1)} e^{i(\varphi_{\mathbf{k}} - \varphi_{\mathbf{q}-\mathbf{k}})}, \tag{37}$$

with

$$\begin{aligned} \Gamma^{(0)} &= \frac{\hbar}{\pi N_F \tau} \frac{1}{g_0 + \left(\frac{1}{g_1} + 1\right) Q^2}, \\ \Gamma^{(1)} &= \frac{\hbar}{\pi N_F \tau} \frac{1}{g_1 + \left(1 + \frac{1}{g_0} + \frac{1}{g_2}\right) Q^2}. \end{aligned} \tag{38}$$

For $q \ll k_F$, it becomes approximately only a function of q,

$$\Gamma(\mathbf{q}) \approx \frac{\hbar}{\pi N_F \tau} \left[\frac{1}{g_0 + \left(\frac{1}{g_1} + 1\right) Q^2} - \frac{1}{g_1 + \left(1 + \frac{1}{g_0} + \frac{1}{g_2}\right) Q^2} \right]. \tag{39}$$

G. Quantum interference correction to conductivity at zero field $\sigma^F(0)$

Put Eq. (39) into Eq. (26), the zero-field quantum interference correction to conductivity can be found as

$$\begin{aligned} \sigma^F(0) &= -\frac{e^2}{\pi h} \sum_{i=0,1} \int_{\ell_\phi^{-2}}^{\ell_e^{-2}} d(q^2) \frac{\alpha_i}{\ell_i^{-2} + q^2} \\ &= -\frac{e^2}{\pi h} \sum_{i=0,1} \alpha_i \ln \frac{\ell_i^{-2} + \ell_e^{-2}}{\ell_i^{-2} + \ell_\phi^{-2}}, \end{aligned} \tag{40}$$

with

$$\begin{aligned} \alpha_0 &= \frac{\eta_v^2 (1 + 2\eta_H)}{2\left(1 + \frac{1}{g_1}\right)}, \quad \ell_0^{-2} = \frac{g_0}{2\ell^2 \sin^2\theta \left(1 + \frac{1}{g_1}\right)}, \\ \alpha_1 &= -\frac{\eta_v^2 (1 + 2\eta_H)}{2\left(1 + \frac{1}{g_0} + \frac{1}{g_2}\right)}, \quad \ell_1^{-2} = \frac{g_1}{2\ell^2 \sin^2\theta \left(1 + \frac{1}{g_0} + \frac{1}{g_2}\right)}, \end{aligned} \tag{41}$$

and $\ell = \sqrt{D\tau}$. The quantum diffusion condition is reflected in the upper bound $q_{\max} = \ell_e^{-1}$ and the lower bound $q_{\min} = \ell_\phi^{-1}$ of the integration over q.

H. Magnetoconductivity $\Delta\sigma(B)$

In the presence of a perpendicular magnetic field B, the finite-field conductivity correction $\sigma^F(B)$ can be derived by replacing q^2 in Eq. (40) with $q_n^2 = (n + \frac{1}{2})/\ell_B^2$, where n labels the Landau levels for 2D massive Dirac fermions and $\ell_B = \sqrt{\hbar/4eB}$ is defined as the magnetic length for a Cooperon. Therefore the finite-field conductivity correction becomes

$$\begin{aligned} \sigma^F(B) = -\frac{e^2}{\pi h} \sum_{i=0,1} \alpha_i \Bigg[&\Psi\left(\frac{\ell_B^2}{\ell_e^2} + \frac{\ell_B^2}{\ell_i^2} + \frac{1}{2}\right) \\ &- \Psi\left(\frac{\ell_B^2}{\ell_\phi^2} + \frac{\ell_B^2}{\ell_i^2} + \frac{1}{2}\right) \Bigg], \end{aligned} \tag{42}$$

where Ψ is the digamma function. The magnetoconductivity is found as

$$\begin{aligned} \Delta\sigma(B) &\equiv \sigma^F(B) - \sigma^F(0) \\ &= \frac{e^2}{\pi h} \sum_{i=0,1} \alpha_i \left[\Psi\left(\frac{\ell_B^2}{\ell_\phi^2} + \frac{\ell_B^2}{\ell_i^2} + \frac{1}{2}\right) - \ln\left(\frac{\ell_B^2}{\ell_i^2} + \frac{\ell_B^2}{\ell_\phi^2}\right) \right], \end{aligned} \tag{43}$$

where we have assumed small magnetic field limit, in which $\ell_B \gg \ell_e$ and

$$\Psi\left(\frac{\ell_B^2}{\ell_e^2} + \frac{\ell_B^2}{\ell_i^2} + \frac{1}{2}\right) \approx \ln\left(\frac{\ell_B^2}{\ell_e^2} + \frac{\ell_B^2}{\ell_i^2}\right). \tag{44}$$

By defining two effective phase coherence lengths $\ell_{\rm L}$ and $\ell_{\rm AL}$,

$$\frac{1}{\ell_{\rm L}^2} \equiv \frac{1}{\ell_0^2} + \frac{1}{\ell_\phi^2}, \quad \frac{1}{\ell_{\rm AL}^2} \equiv \frac{1}{\ell_1^2} + \frac{1}{\ell_\phi^2}, \tag{45}$$

the magnetoconductivity can be written as

$$\Delta\sigma(B) = \frac{e^2}{\pi h} \sum_{i={\rm L,AL}} \alpha_i \left[\Psi\left(\frac{\ell_B^2}{\ell_i^2} + \frac{1}{2}\right) - \ln\left(\frac{\ell_B^2}{\ell_i^2}\right) \right], \tag{46}$$

where $\alpha_{\rm L,AL}$ are given by $\alpha_{0,1}$ in Eq. (41).

I. Singlet and triplet Cooperon channels

In this section we provide an understanding to the vertex function of the maximally crossed diagram Γ from the view of singlet and triplet Cooperon channels. The Bethe-Salpeter equations of the vertex function are equivalent to the diffusion equations of Cooperons. The coordinates of Cooperons are given by the summations of the quantum numbers (momentum, spin,. . .) on the incoming and outgoing sides of the vertex function. It is like to pair two spin-1/2 particles, and the

TABLE II. Cooperon channels for the conventional electrons and Dirac fermions. Triplet (singlet) channel gives WL (WAL). Spin-orbit scattering only quenches the triplet channels, leading to the crossover from WL to WAL for conventional electrons and the suppression of WL in the large-mass limit of Dirac fermions. γ is the Berry phase.

Cooperon channels	Triplet ($\Rightarrow$WL)	Singlet ($\Rightarrow$WAL)
Conventional electron	$\times 3$	$\times 1$
Massless Dirac fermion ($\gamma = \pi$)		$\times 1$
Large-mass Dirac fermion ($\gamma \to 0$)	$\times 1$	

TABLE III. Two-dimensional quantum diffusive transport of conventional and Dirac fermions for impurities of orthogonal (elastic), unitary (magnetic), and symplectic (spin-orbit) symmetries.[42] τ_m and τ_{so} are magnetic and spin-orbit scattering times, respectively. Elastic scattering ($1/\tau_e \neq 0$) is present in all the cases. γ is the Berry phase.

	Orthogonal ($1/\tau_m = 1/\tau_{so} = 0$)	Unitary ($1/\tau_m \neq 0, 1/\tau_{so} = 0$)	Symplectic ($1/\tau_m = 0, 1/\tau_{so} \neq 0$)
Conventional electron	WL	both suppressed	WL → WAL
Massless Dirac fermion $\gamma = \pi$	WAL	suppressed WAL	WAL
Massive Dirac fermion $\gamma \in (0,\pi)$	WAL → WL	both suppressed	WAL or suppressed WL depending on γ
Dirac fermion in large-mass limit $\gamma = 0$	WL	suppressed WL	suppressed WL

coupled spin states are given by the singlet and triplets

$$\begin{aligned} |1,1\rangle &= |\uparrow\rangle \otimes |\uparrow\rangle, \quad |1,-1\rangle = |\downarrow\rangle \otimes |\downarrow\rangle, \\ |1,0\rangle &= \frac{1}{\sqrt{2}}(|\uparrow\rangle \otimes |\downarrow\rangle + |\downarrow\rangle \otimes |\uparrow\rangle), \\ |0,0\rangle &= \frac{1}{\sqrt{2}}(|\uparrow\rangle \otimes |\downarrow\rangle - |\downarrow\rangle \otimes |\uparrow\rangle), \end{aligned} \tag{47}$$

where $|j,m\rangle$ labels the total spin angular momentum j and its z component m.

The Cooperon vertex function Γ can be expressed as a tensor operator acting on the states at the four corners of its diagram in Fig. 9, and

$$\Gamma_{\mathbf{k}_\alpha \mathbf{k}_\beta} = \langle \psi_{\mathbf{k}_\beta}| \otimes \langle \psi_{\mathbf{q}-\mathbf{k}_\beta}|\hat{\Gamma}|\psi_{\mathbf{k}_\alpha}\rangle \otimes |\psi_{\mathbf{q}-\mathbf{k}_\alpha}\rangle. \tag{48}$$

By substituting the eigenstates defined in Eq. (4) for $\mathbf{q} \to 0$, the vertex function becomes

$$\begin{aligned} \Gamma_{\mathbf{k}_\alpha \mathbf{k}_\beta} &= a^4\langle 1,1|\hat{\Gamma}|1,1\rangle + 2a^2b^2 e^{i(\varphi_\alpha - \varphi_\beta)}\langle 0,0|\hat{\Gamma}|0,0\rangle \\ &\quad + b^4 e^{2i(\varphi_\alpha - \varphi_\beta)}\langle 1,-1|\hat{\Gamma}|1,-1\rangle, \end{aligned} \tag{49}$$

where we have used the definition in Eq. (47) and neglected the terms with factors $e^{i(n\varphi_\alpha - m\varphi_\beta)}$ for $m \neq n$. Comparing this expression with Eqs. (30) and (35), we find that

$$\begin{aligned} Z_{00} &= a^4\langle 1,1|\hat{\Gamma}|1,1\rangle, \\ Z_{11} &= 2a^2b^2\langle 0,0|\hat{\Gamma}|0,0\rangle, \\ Z_{22} &= b^4\langle 1,-1|\hat{\Gamma}|1,-1\rangle. \end{aligned} \tag{50}$$

This means that the diagonal terms Z_{00} and Z_{22} come from the triplet Cooperon channels, while Z_{11} from the singlet.

V. CONCLUSIONS

To summarize, Tables II and III compare the 2D massive Dirac fermion and conventional electron in terms of the diffusion of Cooperons. Weak antilocalization results from the singlet Cooperon and weak localization from triplet Cooperons. For 2D conventional electrons, there are two spin-degenerate bands at the Fermi surface, giving rise to one singlet and three triplet Cooperon channels. Spin-orbit scattering can suppress the triplet Cooperons, leading to a crossover from weak localization to weak antilocalization. In contrast, 2D Dirac fermions have only one spin-polarized band at the Fermi surface. In the massless limit, the in-plane spin-momentum locking requires spin to be flipped after backscattering. The summation of incoming and outgoing spins is 0, leading to the weak antilocalization from the singlet Cooperon. In the large-mass limit, spin is polarized along the z axis, the total spin before and after backscattering is 1, corresponding to one of the triplet Cooperons that give weak localization. Due to its nonzero angular momentum, the "triplet" is vulnerable to spin-orbit scattering. The suppressed triplet is accompanied by a crossover from the weak localization into the unitary regime with ignorable magnetoconductivity. Compared with the spin-orbit scattering, the magnetic scattering only induces the crossover to the unitary regime in either weak localization or antilocalization regime.

ACKNOWLEDGMENTS

This work is supported by the Research Grant Council of Hong Kong under Grant No. HKU 7051/10P and HKU UGC Seed Funding Programme for Basic Research No. 201206159001.

*luhz@hku.hk

[1] M. Z. Hasan and C. L. Kane, Rev. Mod. Phys. **82**, 3045 (2010).
[2] X. L. Qi and S. C. Zhang, Rev. Mod. Phys. **83**, 1057 (2011).
[3] J. E. Moore, Nature (London) **464**, 194 (2010).
[4] J. G. Checkelsky, Y. S. Hor, M. H. Liu, D. X. Qu, R. J. Cava, and N. P. Ong, Phys. Rev. Lett. **103**, 246601 (2009).
[5] H. L. Peng, K. J. Lai, D. S. Kong, S. Meister, Y. L. Chen, X. L. Qi, S. C. Zhang, Z. X. Shen, and Y. Cui, Nature Mater. **9**, 225 (2010).
[6] J. Chen, H. J. Qin, F. Yang, J. Liu, T. Guan, F. M. Qu, G. H. Zhang, J. R. Shi, X. C. Xie, C. L. Yang, K. H. Wu, Y. Q. Li, and L. Lu, Phys. Rev. Lett. **105**, 176602 (2010).
[7] J. G. Checkelsky, Y. S. Hor, R. J. Cava, and N. P. Ong, Phys. Rev. Lett. **106**, 196801 (2011).
[8] H. T. He, G. Wang, T. Zhang, I. K. Sou, G. K. L. Wong, J. N. Wang, H. Z. Lu, S. Q. Shen, and F. C. Zhang, Phys. Rev. Lett. **106**, 166805 (2011).
[9] M. H. Liu, C. Z. Chang, Z. C. Zhang, Y. Zhang, W. Ruan, K. He, L. L. Wang, X. Chen, J. F. Jia, S. C. Zhang, Q. K. Xue, X. C. Ma, and Y. Y. Wang, Phys. Rev. B **83**, 165440 (2011).
[10] J. Wang, A. M. DaSilva, C. Z. Chang, K. He, J. K. Jain, N. Samarth, X. C. Ma, Q. K. Xue, and M. H. W. Chan, Phys. Rev. B **83**, 245438 (2011).

[11]M. H. Liu, J. S. Zhang, C. Z. Chang, Z. C. Zhang, X. Feng, K. Li, K. He, L. L. Wang, X. Chen, X. Dai, Z. Fang, Q. K. Xue, X. C. Ma, and Y. Y. Wang, Phys. Rev. Lett. **108**, 036805 (2012).
[12]J. Chen, X. Y. He, K. H. Wu, Z. Q. Ji, L. Lu, J. R. Shi, J. H. Smet, and Y. Q. Li, Phys. Rev. B **83**, 241304(R) (2011).
[13]Y. S. Kim, M. Brahlek, N. Bansal, E. Edrey, G. A. Kapilevich, K. Iida, M. Tanimura, Y. Horibe, S. W. Cheong, and S. Oh, Phys. Rev. B **84**, 073109 (2011).
[14]H. Steinberg, J. B. Laloë, V. Fatemi, J. S. Moodera, and P. Jarillo-Herrero, Phys. Rev. B **84**, 233101 (2011).
[15]T. Ando, T. Nakanishi, and R. Saito, J. Phys. Soc. Jpn. **67**, 2857 (1998).
[16]D. Hsieh, Y. Xia, D. Qian, L. Wray, J. H. Dil, F. Meier, J. Osterwalder, L. Patthey, J. G. Checkelsky, N. P. Ong, A. V. Fedorov, H. Lin, A. Bansil, D. Grauer, Y. S. Hor, R. J. Cava, and M. Z. Hasan, Nature (London) **460**, 1101 (2009).
[17]S. Hikami, A. Larkin, and Y. Nagaoka, Prog. Theor. Phys. **63**, 707 (1980).
[18]S. Maekawa and H. Fukuyama, J. Phys. Soc. Jpn. **50**, 2516 (1981).
[19]G. Bergmann, Phys. Rev. Lett. **48**, 1046 (1982).
[20]G. Bergmann, Phys. Rep. **107**, 1 (1984).
[21]In the Feynman diagrams for the vertex function of Cooperons, two Green function lines point along the same direction (see Fig. 1), similar to the particle-particle correlation functions for the Cooper pair transport in superconductors.
[22]K. B. Efetov, A. I. Larkin, and D. E. Khemlnitzkii, JETP **52**, 568 (1980).
[23]B. L. Altshuler, A. G. Aronov, A. I. Larkin, and D. E. Khemlnitzkii, JETP **54**, 411 (1981).
[24]A. J. Millis and P. A. Lee, Phys. Rev. B **30**, 6170 (1984).
[25]H. Z. Lu and S. Q. Shen, Phys. Rev. B **84**, 125138 (2011).
[26]H. Z. Lu, W. Y. Shan, W. Yao, Q. Niu, and S. Q. Shen, Phys. Rev. B **81**, 115407 (2010).
[27]W. Y. Shan, H. Z. Lu, and S. Q. Shen, New J. Phys. **12**, 043048 (2010).
[28]Y. Zhang, K. He, C. Z. Chang, C. L. Song, L. L. Wang, X. Chen, J. F. Jia, Z. Fang, X. Dai, W. Y. Shan, S. Q. Shen, Q. Niu, X. L. Qi, S. C. Zhang, X. C. Ma, and Q. K. Xue, Nat. Phys. **6**, 584 (2010).
[29]I. Garate and L. Glazman, Phys. Rev. B **86**, 035422 (2012).
[30]V. K. Dugaev, P. Bruno, and J. Barnas, Phys. Rev. B **64**, 144423 (2001).
[31]B. L. Altshuler, D. Khmel'nitzkii, A. I. Larkin, and P. A. Lee, Phys. Rev. B **22**, 5142 (1980).
[32]J. Rammer, *Quantum Transport Theory* (Westview, Boulder, CO, 2004).
[33]H. Suzuura and T. Ando, Phys. Rev. Lett. **89**, 266603 (2002).
[34]E. McCann, K. Kechedzhi, V. I. Fal'ko, H. Suzuura, T. Ando, and B. L. Altshuler, Phys. Rev. Lett. **97**, 146805 (2006).
[35]N. H. Shon and T. Ando, J. Phys. Soc. Jpn. **67**, 2421 (1998).
[36]H. Z. Lu, J. R. Shi, and S. Q. Shen, Phys. Rev. Lett. **107**, 076801 (2011).
[37]P. Ghaemi, R. S. K. Mong, and J. E. Moore, Phys. Rev. Lett. **105**, 166603 (2010).
[38]K. I. Imura, Y. Kuramoto, and K. Nomura, Phys. Rev. B **80**, 085119 (2009).
[39]I. Garate, J. Sinova, T. Jungwirth, and A. H. MacDonald, Phys. Rev. B **79**, 155207 (2009).
[40]Y. S. Hor, A. Richardella, P. Roushan, Y. Xia, J. G. Checkelsky, A. Yazdani, M. Z. Hasan, N. P. Ong, and R. J. Cava, Phys. Rev. B **79**, 195208 (2009).
[41]D. X. Qu, Y. S. Hor, J. Xiong, R. J. Cava, and N. P. Ong, Science **329**, 821 (2010).
[42]F. J. Dyson, J. Math. Phys. (NY) **3**, 140 (1962).